



HAL
open science

Impact of the coarse indoor non-radioactive aerosols on the background radon progenies' compensation of a continuous air monitor

Gwenaël Hoarau, Gregoire Dougniaux, Francois Gensdarmes, Philippe Cassette, Gilles Ranchoux

► To cite this version:

Gwenaël Hoarau, Gregoire Dougniaux, Francois Gensdarmes, Philippe Cassette, Gilles Ranchoux. Impact of the coarse indoor non-radioactive aerosols on the background radon progenies' compensation of a continuous air monitor. *Health Physics*, 2022, 122 (5), pp.563-574. 10.1097/HP.0000000000001530 . hal-03760074

HAL Id: hal-03760074

<https://hal.science/hal-03760074>

Submitted on 24 Aug 2022

HAL is a multi-disciplinary open access archive for the deposit and dissemination of scientific research documents, whether they are published or not. The documents may come from teaching and research institutions in France or abroad, or from public or private research centers.

L'archive ouverte pluridisciplinaire **HAL**, est destinée au dépôt et à la diffusion de documents scientifiques de niveau recherche, publiés ou non, émanant des établissements d'enseignement et de recherche français ou étrangers, des laboratoires publics ou privés.

ARTICLE COVERSHEET
LWW_CONDENSED(8.125X10.875)
SERVER-BASED

Article : HPJ_210121

Creator : apps_lww

Date : Wednesday January 19th 2022

Time : 03:39:46

Number of Pages (including this page) : 14

Impact of the Coarse Indoor Non-radioactive Aerosols on the Background Radon Progenies' Compensation of a Continuous Air Monitor

AQ1 Gwenaël Hoarau, Grégoire Dougniaux, François Gensdarmes, Philippe Cassette, and Gilles Ranchoux¹

INTRODUCTION

Abstract—This paper addresses the problem of false positive alarm when using a continuous air monitor (CAM) in decommissioning sites of nuclear facilities. CAMs are used to measure airborne activity and play an important role in the radiation protection of workers likely to be exposed to radioactive aerosols. Monitors usually sample aerosols on a membrane filter. Radioactive particles sampled are detected through the alpha and beta decays that they emit. These latter ionizing particles are measured online by spectrometry thanks to a Passivated Implanted Planar Silicon detector (PIPS). Alpha and beta decays, in this context, come mainly from the natural radon progeny (^{218}Po , ^{214}Pb , and so on) and, in the case of radioactive contamination, also from artificial radionuclides such as ^{239}Pu or ^{137}Cs . The aim of the CAM is to alert the workers when the artificial airborne activity occurs, always considering the presence of a variable background due to the natural particulate airborne activity. The CAM-specific algorithm considers this background dynamically and continuously, often by using a constant parameter. However, non-radioactive aerosols are also sampled on the membrane filter. These latter make the discrimination more difficult as they lead to the deterioration of the alpha-energy spectrum. In this paper, the impact of the non-radioactive aerosols sampled by the CAM on its behavior is highlighted for four aerosol size distributions. The evolution of the background is characterized as a function of the aerosol mass sampled, with the example of a simple algorithm. Thus, in this paper, results show a positive correlation of the background with the aerosol mass sampled by the CAM. In addition, results highlight at least two different evolutionary trends according to the aerosol size distribution. An explanation of these evolutions is given by considering the penetration profile of the natural radioactive aerosols in the granular deposit above the CAM filter. The main consequence of these results is that the background could not be considered as proportional to radon progeny as it is currently used.

AQ2

Health Phys. 122(00):000–000; 2022

Key words: aerosols; monitors, radiation; nuclear power plant; radiation, background

ON-SITE AIRBORNE radioprotection is monitored by so-called continuous air monitors (CAMs). Their goal is to measure continuously and in real time the radioactivity carried by aerosols and trigger an alert whenever the measured activity exceeds a threshold. These CAMs are designed to pump air from the atmosphere and to trap the aerosols on a retaining medium. The detector facing the retaining medium counts the radiations emitted from the collected aerosols. Among collected aerosols, one needs to distinguish:

- those that are produced in nuclear facilities and are the subject of the measurement; they are referred to as radioactive artificial aerosols. Elder et al. (1974) present the different Activity Median Aerodynamic Diameter (AMAD) characteristics of artificial radioactive aerosols in nuclear facilities in case of accidents; and
- those that are due to radon progenies that are produced naturally and are ubiquitous in air.

Instruments that measure radioactive artificial aerosols minimize the influence of natural radioactive aerosols, either physically or by using a signal treatment system. A minimization operated by a physical process using natural radioactivity (radon progeny) is carried by fine and ultra-fine particles, respectively, in size-ranges of 100–300 nm and 0.5–5 nm. The Brownian diffusion through an annular sampling head could be used to remove ultra-fine particles, and following this step, a specific filter with a very low collection efficiency for fine particles could be used to collect only artificial radioactive particles assumed to be in the micro-size range. Such processes using NucleporeTM filters with adequate pore-size and filtration velocity have been proposed by Charreau et al. (1984) and Burghoffer et al. (1987). Another technique using an inlet screen designed to collect ultra-fine radon progeny has been proposed by McFarland et al. (1992).

A minimization operated by a signal treatment system could be based on pseudo alpha-beta coincidence (Klett et al. 1997) or spectral shape treatment, as described in the review paper by Justus (2021).

AQ5

¹IRSN/PSN-RES/SCA, Laboratoire d'Etudes et de Modélisation en Aerodispersion et Confinement Gif-sur-Yvette, Île-de-France, France.

The authors declare no conflicts of interest.

For correspondence contact: Grégoire Dougniaux, IRSN/PSN-RES/SCA: Laboratoire d'Etudes et de Modélisation en Aerodispersion et Confinement Gif-sur-Yvette, Île-de-France, France.

(Manuscript accepted 6 December 2021)

0017-9078/22/0

Copyright © 2022 Health Physics Society

DOI: 10.1097/HP.0000000000001530

www.health-physics.com

The performances of these CAM are assessed by their conformity to standards, notably IEC 60761 and IEC 61578. In order to test the CAM in actual operating conditions, some reference atmospheres are defined in standards. The IEC 61578, referenced by IEC 60761, prescribes the aerosol concentration and size distribution.

On-site aerosol characteristics measurements have highlighted significant discrepancies with the standards. Indeed, a measurement process used in dismantling a nuclear facility site (Dougnaux et al. 2016) has focused attention on:

- the presence of coarse particles, thus a non-standard size distribution; and
- the swiftness of the particle concentration variation, thus a non-standard concentration.

The influence due to airborne non-radioactive aerosol on the CAM measurements has been observed during basic operations, like cleaning or cutting. Moreover, during these kinds of operations, a CAM sometimes triggered alarms without any artificial radioactivity. These events caused the operators to measure some characteristics of the collected aerosols. On the one hand, nuclear measurements only show the presence of radon progenies. On the other hand, mass measurements show a large amount of collected non-radioactive aerosols. Experiments have been conducted by several authors to appreciate the effect of the aerosol mass deposit on the nuclear measurement (Bartlett and Walker 1996; Geryes and Monsanglant-Louvet 2011; Hogue et al. 2018; Hoover and Newton 1998; Huang et al. 2002; Moore et al. 1993; Seiler et al. 1988). The experiments showed the influence of the amount of material on the nuclear, especially alpha, measurement, which is significantly degraded, and the result given by the CAM got worse with the aerosol mass

AQ6 accumulation on the sampling filter. However, no experimentation has yet considered the non-radioactive aerosol size distributions, and no relationship between the aerosol characteristics and the CAM measurement have been highlighted. Indeed, the radon progeny are mainly attached to an aerosol whose activity median aerodynamic diameter is about 0.2 μm ; and the coarse aerosol, non-radioactive median aerodynamic diameter is more than 5 μm . This leads to the need for a complementary evaluation of the effectiveness of radon progeny compensation, continuously and in real time, with various atmospheres, e.g., those on nuclear dismantling sites.

In this study, the CAM sampling head faces the simulated dismantling atmospheres (produced inside a specific bench), and its behavior is evaluated through the evolution of the crosstalk between two close regions of interest (ROI) in terms of energy spectra measured by the CAM. The aim of this CAM algorithm is to determine the background value in the artificial-alpha region based on the information in the natural-alpha region. For that purpose, we used a simple two-region algorithm (Justus 2011). The true

algorithm of a CAM is not available from the manufacturer and is not necessary to our study. Thereby, the first ROI is dedicated to containing the artificial alpha emitters, such as ^{239}Pu or ^{241}Am , and the second ROI is dedicated to containing mainly ^{218}Po . The background in the first ROI is considered proportional to the total counts measured in the second ROI. The proportional coefficient is determined by the manufacturer for all exposure situations and confirmed experimentally for IEC standard conditions. One can notice that spectral treatment methods based on tail- or peak-fitting could be used to determine the coefficient values. The coefficient value is highly dependent on the defined ROI and algorithm and, of course, on the CAM geometry (sampling head's Si detector active area, the filter's active area, the air gap, collimation grids, sampling filter property, etc.). Therefore, the coefficient values provided in this paper are specific to the CAM studied ².

The following discusses the influence of the non-radioactive aerosol mass and size distribution sampled by the CAM on the crosstalk evolution between the two ROIs. More specifically, the evolution of the coefficient for non-standard IEC condition is studied thanks to the non-radioactive aerosol size distribution and mass collected on the sampling filter.

MATERIALS AND METHODS

Bench tests—ICARE + EAC

The specific atmospheres are produced thanks to the ICARE bench test with specific experimental tools added—the first for ensuring a stable generation of natural radioactive aerosols, and the second for the generation of non-radioactive aerosols in various concentrations and size distributions.

ICARE is a unique facility for generating calibrated radioactive aerosols (Ammerich 1988; Monsanglant-Louvet et al. 2012; Zettwoog 1990) with activity median aerodynamic diameters (AMAD) from 0.1 to 10 μm and volume activities up to 200 Bq m^{-3} . The aerosols are tagged with various nuclides, from natural (such as ^{222}Rn daughters) to anthropogenic nuclides (such as ^{137}Cs or ^{239}Pu). The natural airborne radioactivity used is composed of ^{222}Rn (gas) plus 80% of the attached fraction (AMAD of 0.2 μm) and 20% of the unattached fraction (atomic size). This atmosphere is stable during the experiments. The reference activities for ^{222}Rn and progeny are measured using Thomas' (1972) method: 30 Bq m^{-3} for ^{222}Rn , 12 Bq m^{-3} for ^{218}Po , and 5 Bq m^{-3} for ^{214}Po . Nevertheless, ICARE must be extended to produce the coarse non-radioactive aerosols.

We designed a specific extension for ICARE, designed to generate and resuspend non-radioactive aerosols, called

²Mirion Technology. ABPM203M Mobile Alpha Beta Particulate Monitor (n.d.)

F1 the experimental aerosol chamber (EAC), depicted in Fig. 1. It is composed of:

- a coarse aerosol generator and a rotative brush generator (RBG);
- an optical particle counter (OPC), which monitors the effective aerosol characteristics (size distribution and concentration); and
- a HEPA filter-flowmeter-pump assembly that provides the ability to control the evolution of the non-radioactive aerosol concentration produced inside the chamber (i.e., either fast or slow variation of aerosol concentration is reachable).

The EAC allows the production of atmospheres with calibrated non-radioactive aerosols with diameters up to $60\ \mu\text{m}$ and concentrations up to $50\ \text{Bq m}^{-3}$, values observed on dismantling nuclear sites (Doughniaux et al. 2016).

The qualification of the EAC ensured that the conditions reproduced in the experimental chamber are representative of those that can be encountered in a nuclear dismantling site, as depicted in the study (Doughniaux et al. 2016). The specific qualification process was based on three parameters: the aerosol size distribution injected and sampled, the variability in aerosol concentration produced and injected, and finally the homogeneity of the aerosol concentration in the chamber. The result of the experimental validation of the device was presented at the French Congress on Aerosols 2019 (CFA 2019) by Hoarau et al. (2019).

Non-radioactive aerosol characteristics

We define the best simulant aerosol as one that mimics those measured in nuclear dismantling sites according to three criteria:

- wide range in aerosol size distribution allowing simulation of an equally wide diversity of atmospheric conditions;
- irregular particle shape; and
- density close to that of aerosols measured in a nuclear dismantling site (mainly from 2 to $6\ \text{g cm}^{-3}$).

Alumina powder (Al_2O_3), combining these three criteria with a density of $3.95\ \text{g cm}^{-3}$, was chosen for the study. Fig. **F2** 2 represents an alumina aerosol deposit on a membrane filter taken with a scanning electron microscope (SEM).

In order to cover a wide range of size-dimension, we used four alumina powders, lettered from A to D, with mass median aerodynamic diameters from 9 to $56.9\ \mu\text{m}$.

To characterize the aerosol behavior, two related parameters are needed. The first is the mass median aerodynamic diameter. It is well suited to study the particle behavior in the air, i.e., from the injection of alumina aerosols inside the EAC to the sampling achieved by the CAM. The second parameter is the mass median volume equivalent diameter (MMV_{eqD}). It is appropriate to characterize the particle deposit (thickness, porosity, etc.) and the alpha particle energy loss in matter. The MMV_{eqD} is calculated by using eqn (1), which considers four parameters: the Cunningham

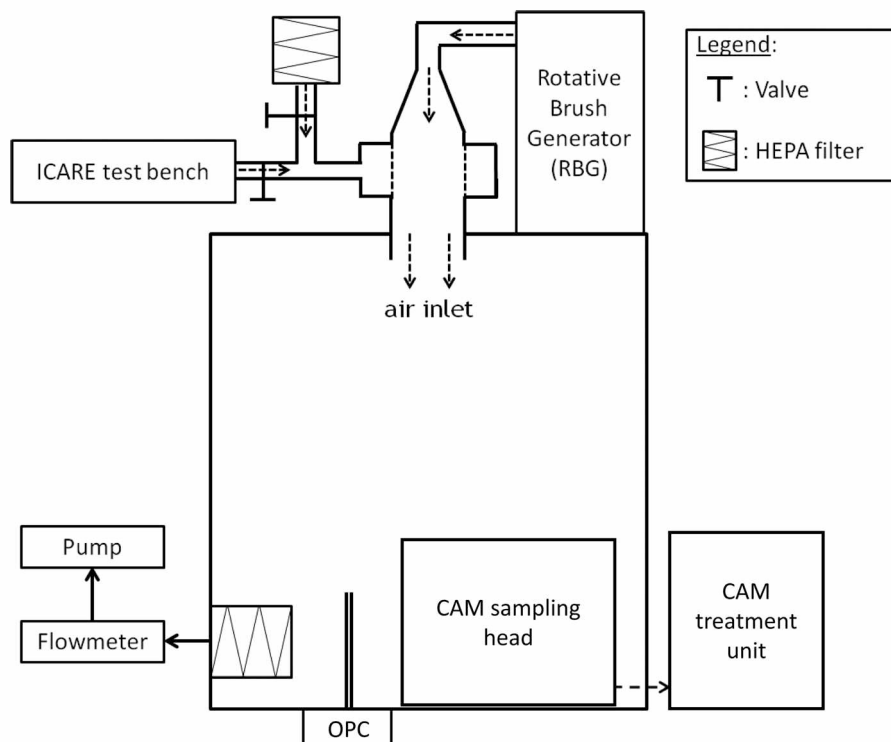


Fig. 1. Experimental aerosol chamber (EAC) with the CAM sampling head exposed inside the volume.

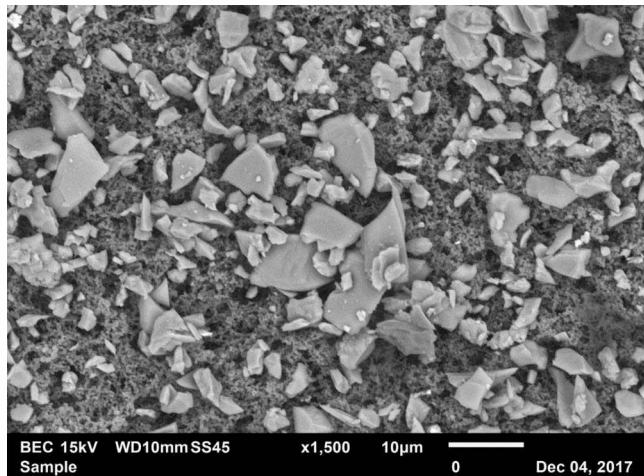


Fig. 2. Alumina (Al_2O_3) aerosols, sampled and collected on a membrane filter, observed with a scanning electron microscopy (SEM).

factor C_u , the particle density ρ , the dynamic shape factor χ , and the MMAD. The Cunningham factor for the aerodynamic and volume equivalent diameter is approximated to unity as the non-radioactive particle diameter in this study and is always superior to $5 \mu\text{m}$ (Baron and Willeke, 2001). The dynamic shape factor for alumina aerosols is taken from the literature (Mark et al. 1985; Witschger et al. 2002, 2004):

$$\text{MMV}_{\text{eqD}} = \sqrt{\frac{C_u(d_a)\rho_0\chi}{C_u(d_{\text{veq}})\rho}} \text{MMAD}, \quad (1)$$

where $C_u(d_a)$ and $C_u(d_{\text{veq}})$ = Cunningham factor, respectively, for aerodynamic and volume equivalent diameter; ρ_0 is the standard density (1 g cm^{-3}); ρ is particle density (3.95 g cm^{-3}); and φ is the dynamic shape factor.

The size distributions of the particles sampled by the **AQ8** CAM were analyzed by an Aerosizer (PSD 3603, TSI). The results are then corrected for the bias inherent to the measurement of non-spherical particles by the Aerosizer. Indeed, studies of Cheng et al. (1993) have highlighted that the Aerosizer could underestimate the particle size distribution from 20 to 50% for non-spherical particles. Our laboratory has specifically quantified this bias for alumina particles used by comparing the Aerosizer measurement results with those obtained with the Coulter technique. For the alumina powder used in this study, the Aerosizer underestimated the conventionally true MMAD by 32%. The correct values of MMAD for the four aerosols used in this study are reported in **Table 1**.

CAM working principle

During this study, we used a ABPM203M (Mirion Technology), referred to in this paper by the generic term “CAM.” The quantified results we present are thus linked

to this specific monitor. It was loaned by EDF, and Mirion is not involved in this study.

The general operating principle of the CAM is depicted in Fig. 3. It can be explained in three separate parts, but they run in a linked way. The first part, corresponding to the input parameters, is associated with the sampling head of the CAM. This latter is directly exposed to the atmospheric conditions produced in the chamber of the EAC (and close to the worker in a real situation). Analyses and processes correspond to the most technical part with the algorithm of the CAM, which is usually established by the manufacturer. This part achieves calculations to reach the radioactivity from the aerosols sampled in the first step. In the end, the calculated activity concentrations are screened out at every time step.

The CAM performs pseudo-continuous measurement: the base time unit is 3 s for the CAM we used. In 3 s, the CAM realizes all the stages of its measurement loop. For the tests we wanted to perform on the CAM, it was impossible to obtain good measurements in the same period; therefore, the data treatments were achieved on the experimental spectra after 2 h of measurement. The results are thus based on 2 h of aerosol accumulation on the CAM sampling filter.

Aerosols sampling and nuclear measurements—input parameters. In Fig. 4, a schema on the CAM sampling head is depicted. The natural radioactive particles are represented with the small-dashed spheres (\otimes), while the black spheres (\bullet) are the non-radioactive aerosols. The black dashed lines represent the fluid streamlines. The full black arrows represent the direction of some alpha particles to the nuclear detector. The radioactive aerosols are measured with a spectroscopic acquisition chain to get a characteristic energy spectrum.

Fig. 5 presents an example of two energy spectra measured by the CAM for 2 h. Measured radioactivity comes from natural airborne activity ($A_{222\text{Rn}} = 30 \text{ Bq m}^{-3}$, $A_{218\text{Po}} = 12 \text{ Bq m}^{-3}$ and $A_{214\text{Po}} = 5 \text{ Bq m}^{-3}$). The differences between the two spectra come from the coarse non-radioactive aerosol: the spectrum in black dots is measured under IEC standard conditions, while the spectrum in black line is measured under dismantling of nuclear facility site conditions, simulated inside the EAC. The particle masses sampled by the CAM are calculated at about $2 \mu\text{g}$ in the

Table 1. Characteristics of the particles size distribution studied.

	A	B	C	D
MMAD (μm)	9.0	12.8	17.8	56.9
Geometric standard deviation	1.86	1.76	1.30	1.39
χ – Dynamic shape factor	1.55	1.50	1.60	1.20
MMV_{eqD} (μm)	5.7	7.9	11.3	31.4

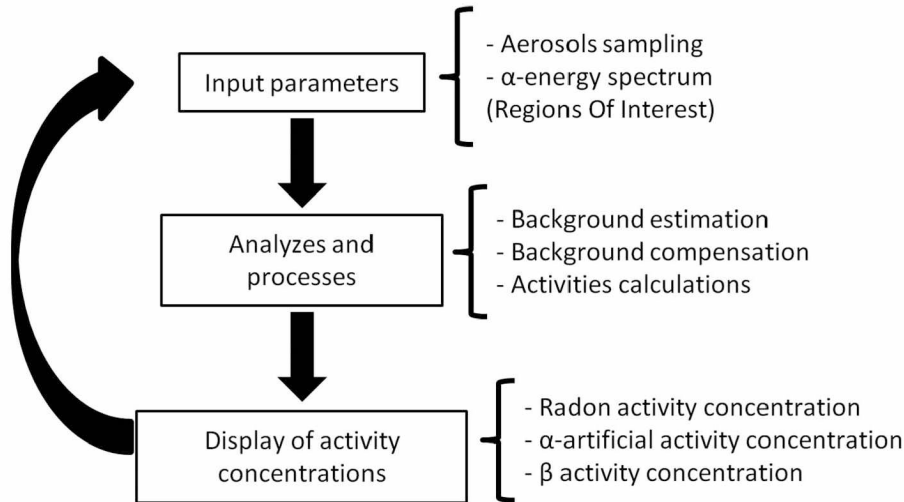


Fig. 3. The three main linked parts illustrating the general operating principle of the CAM.

IEC standard test condition and measured to 3.9 mg in the dismantling site condition. The spectra shapes are both different but reveal characteristic peaks related to ubiquitous occurrence of radon progenies (essentially ^{218}Po , ^{214}Po) in the air.

For the analyses produced by the CAM, the spectrum is divided into three main regions of interest (ROI) in order to discriminate the natural activity from the artificial. This process is used by the ABPM203M. The defined ROI used by the CAM are summarized in Table 2. The ROI boundary energies were extracted from the CAM itself. One of the reasons for this spectrum splitting is to be able to identify the contribution of the natural radioactive aerosols in the artificial radioactive aerosol energy area. Indeed, the energy deposition for one radiation in the detector ranges between 0 and $E_{\alpha\text{particle}}$. Due to the design of the sampling head of the CAM, radiations undergo a systematic attenuation in the air. This is the reason why the energy range of each ROI is lower than the energies of the alpha particle emission. Thus, in the present paper, we always refer to the deposited energy as measured by the instrument and not the initial emitted energy.

Analyses and processes—treatment algorithm. The treatment algorithm of the CAM runs in real time to calculate the activity concentrations corresponding to the radon and to the artificial airborne activity. These activity concentrations are calculated by considering the increased counts measured in the associated ROI. Particularly for alpha-artificial airborne activity, the treatment algorithm must consider the background in the ROI1, which can be significant and dependent on the exposure situation. The background in this energy range being mainly due to the radon progeny (^{218}Po), an automatic process is used to subtract it. The net count in ROI1 is calculated using eqn (2), which is a simpler form of the equation expressed by Li et al. (2013), similar to the 2-ROI algorithm developed for Eberline monitors in the 1980s:

$$N_{\text{artificial}} = N_1 - K N_2, \quad (2)$$

where:

N_1 and N_2

$N_{\text{artificial}}$ = the net counts in ROI1 (due to alpha-artificial radionuclides only);

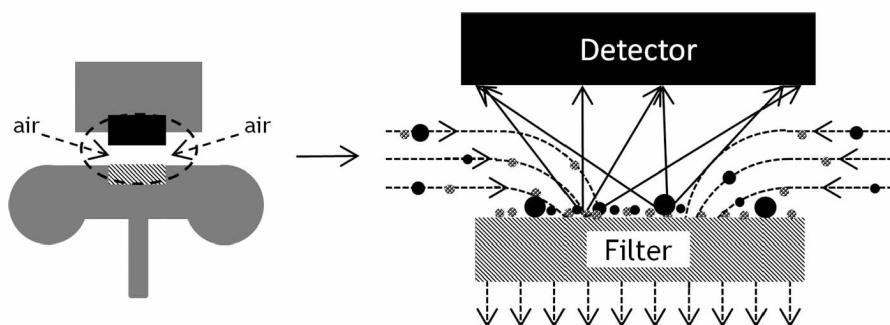


Fig. 4. Magnification on the sampling head of the CAM for showing both the direction of the fluid streamlines and how particles are sampled on a filter. The small, dashed spheres (⊗) and the black (●) spheres are, respectively, the natural radioactive and non-radioactive particles. The full black arrows indicate the direction of radiation to the detector, while the black dashed lines indicate the fluid streamlines.

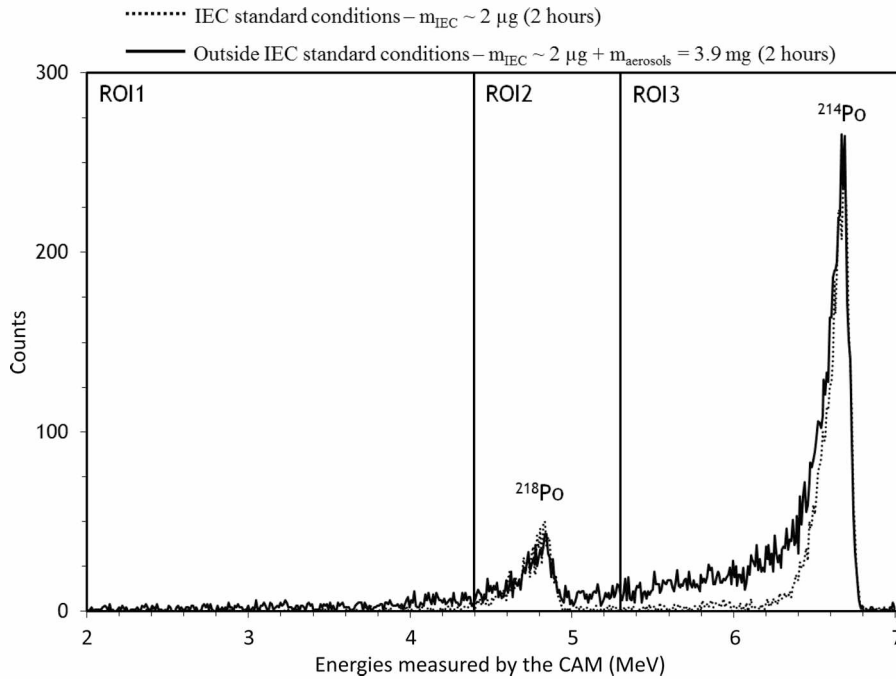


Fig. 5. Energy spectra measured by the CAM under IEC standard condition (in black dots) and under simulated dismantling site conditions (in full black line). The spectrum is divided into three ROIs where the radionuclides are expected as mentioned in Table 2.

N_1 and N_2 = the gross counts in ROI1 and ROI2, respectively; and

K = the proportion of ^{218}Po and ^{214}Po radon progeny counts measured in the ROI1 due to the deterioration of the energy spectrum (i.e., the ratio of the total count measured in ROI1 to the total count measured in ROI2 for a period of time).

The K parameter value is determined under IEC standard conditions ($K = 0.09$ for the CAM used) and applied for all exposure situations. The K value is highly dependent on the defined ROI and algorithm and of course on the CAM geometry (sampling head's Si detector active area, the filter's active area, the air gap, collimation grids, sampling filter property, etc.). Therefore, the K value provided in this paper is specific to the CAM studied. Alpha-artificial airborne activity concentration (Bq m^{-3}) is calculated from eqn (3) (Li et al. 2013):

$$C_{\text{artificial}} = \frac{N_{\text{artificial}}}{\varepsilon_T Q_V t_1 t_2} = \frac{N_{\text{artificial}}}{\varepsilon_T Q_V t^2} = \frac{N_1 - K N_2}{\varepsilon_T Q_V t^2}, \quad (3)$$

where ε_T is the CAM absolute detection efficiency, Q_V = CAM flow rate ($\text{m}^3 \text{s}^{-1}$), and t_1 and t_2 , respectively, are the sampling time and the counting time (s).

In the end, the alpha-artificial airborne activity concentration is compared to a critical level defined by equation 4 from Li et al. (2013), to assess whether the alpha-artificial radionuclides are present or not. If $C_{\text{artificial}}$ is greater than $C_{\text{threshold}}$, an alarm is triggered to warn the worker that alpha-artificial radionuclides are present in the air:

$$C_{\text{threshold}} = k_{\alpha} \frac{\sqrt{N_{\text{artificial}}}}{\varepsilon_T Q_V t^2}, \quad (4)$$

where k_{α} is the number of standard deviations of a Gaussian distribution. Thus, k_{α} corresponds to a risk acceptance level, which is directly linked to the false alarm probability. Consequently, if the background compensation is not suitable (i.e., a variation of N_2 incorrectly compensated with K), then the alpha-artificial airborne activity may be overestimated. If this overestimation is above the

Table 2. Radionuclides contributing in ROI1, ROI2 and ROI3 are mentioned with their half-life ($T_{1/2}$) and main alpha-energy E_{α} (Laraweb 2017).

Region of Interest (ROI)	Energy range (MeV)		Main radionuclides
1	2 – 4.4	Artificial	^{239}Pu ($T_{1/2} = 24.103$ y, $E_{\alpha} = 5.2$ MeV) ^{241}Am ($T_{1/2} = 432$ y, $E_{\alpha} = 5.5$ MeV)
2	4.4 – 5.3	Natural	^{218}Po ($T_{1/2} = 3.071$ min, $E_{\alpha} = 6.0$ MeV) ^{212}Bi ($T_{1/2} = 60.54$ min, $E_{\alpha} = 6.0$ MeV)
3	5.3 – 7		^{214}Po ($T_{1/2} = 162$ μs , $E_{\alpha} = 7.7$ MeV)

defined critical level, an alarm is triggered; this is a false positive.

Procedure for characterizing the evolution of the K parameter

The CAM was faced toward different atmospheric conditions in the EAC using four different aerosol characteristics (Table 1). Several experiments were carried out for each of the four aerosols. An experiment is constituted of two parts of 2 h each:

- **First part:** The valve associated with the HEPA filter in the upper part of the EAC (see Fig. 1) is closed, and the RBG is off. Only the valve associated with the ICARE test bench is opened, and the ICARE test bench is on. During this first part, only a stable natural radioactive aerosol is sampled in the chamber of the EAC by the CAM and the OPC at 35 L min^{-1} and 1.2 L min^{-1} , respectively. This part is useful to have a homogeneous natural radioactive aerosol concentration in the chamber, which takes about 10 min^3 and to stabilize the measurement achieved by the CAM under standard conditions.
- **Second part:** the valve associated with the HEPA filter in the upper part of the EAC (see Fig. 1) is closed, and the one associated with the ICARE test bench is opened. In this part, the RBG is switched on for varying durations (in a range of 10 s to 10 min) in order to reproduce non-radioactive aerosol puffs mixed to the natural radioactive aerosols sampled in the chamber of the EAC. In the lower part of the EAC, the OPC and the CAM are on.

During this second part, the OPC and the CAM sample the air at the same flow rates as indicated above. After certain generation duration, the RBG is switched off, and the valve associated to the HEPA filter (in the upper part of the EAC) is opened. In the lower part of the EAC, the HEPA filter-flowmeter-pump assembly is switched on for a few minutes in order to rapidly reduce the non-radioactive aerosols in the chamber. The sampling achieved by the CAM and the OPC is still ongoing until the end of the experiment.

For each experiment, a blank membrane filter (Millipore FSLW) is placed on the appropriate area of the sampling head of the CAM. This filter is weighed, using an analytical balance, before and after each experiment.

The aerosol mass accumulated during one experiment is then deduced (eqn 5):

$$m_{\text{acc}} = m_{\text{end}} - m_{\text{init}}. \quad (5)$$

After each measurement, the energy spectrum recorded by the CAM is treated to determine the experimental value of

³Three air renewals are necessary to reach a concentration at 95% of equilibrium. The volume of the chamber is 0.122 m^3 , the sampling is achieved at a flow rate of $(35 + 1.2) \text{ L min}^{-1}$, which led to 3 min and 22 s for one air renewal. Thus, about 10 min for three air renewals.

the K parameter related to the aerosol mass sampled by the CAM. This method makes it possible to characterize the evolution of the K parameter over a time step of 2 h.

RESULTS AND DISCUSSION

The results obtained for the four aerosol size distributions are presented in Fig. 6 as a relation between the cumulated mass with the K parameter. The latter is calculated from the spectra recorded by the CAM according to eqn (2). Error bars depicted on each data point correspond to the propagated expanded uncertainties (two standard deviations) in the calculation of the K parameter and assuming the ROI counts follow a Poisson distribution. The masses represent the sum of all aerosols collected on the sampling filter during an experiment. However, one notices that the mass of the natural radioactive aerosols is only about a few micrograms, thus negligible in comparison to the mass of the non-radioactive aerosol.

For the aerosols A & B, a transition zone is distinguishable (Fig. 6) when the MMV_{eqD} of the particles sampled is lower than $10 \mu\text{m}$. Indeed, the value of the K parameter begins to increase slightly relative to the particle mass sampled followed by a sudden upward change in the curve slope. This evolution change asserts that the behavior of the K parameter is not merely impacted by the particle mass sampled on the sampling filter; particle deposition shape is a necessary parameter to consider. The particle deposition can be understood by the packing size porosity and will be introduced later.

For the aerosols C & D, contrary to what was described previously, the value of the K parameter increases suddenly with the particles mass sampled when the MMV_{eqD} of particles is higher than $10 \mu\text{m}$. However, from a value of mass-sampled particles, the K parameter decreases a bit before starting to increase again. This behavior is currently misunderstood, but more data in the declining region (i.e., between 12 and 16 mg for aerosol C and between 8 and 12 mg for aerosol D) are necessary to assert this trend.

The experimental results highlight that the K parameter is not constant, as currently assumed. This is true for the four aerosol size distributions studied; its evolution is significantly influenced both by the mass of particles sampled by the CAM and the aerosol size distributions. Indeed, two different evolution types (i.e., for the K parameter related to the mass of particles sampled) are identified in Fig. 6; one associated to the aerosols A and B with a $\text{MMV}_{\text{eqD}} < 10 \mu\text{m}$ and the other one to aerosol C and D with a $\text{MMV}_{\text{eqD}} > 10 \mu\text{m}$ (see characteristics in Table 1).

Equivalent number of particle layers on the sampling filter

In order to explain the noticeable differences between the four aerosol size distributions, we propose to evaluate the number of layers of particle deposited. Indeed, for a

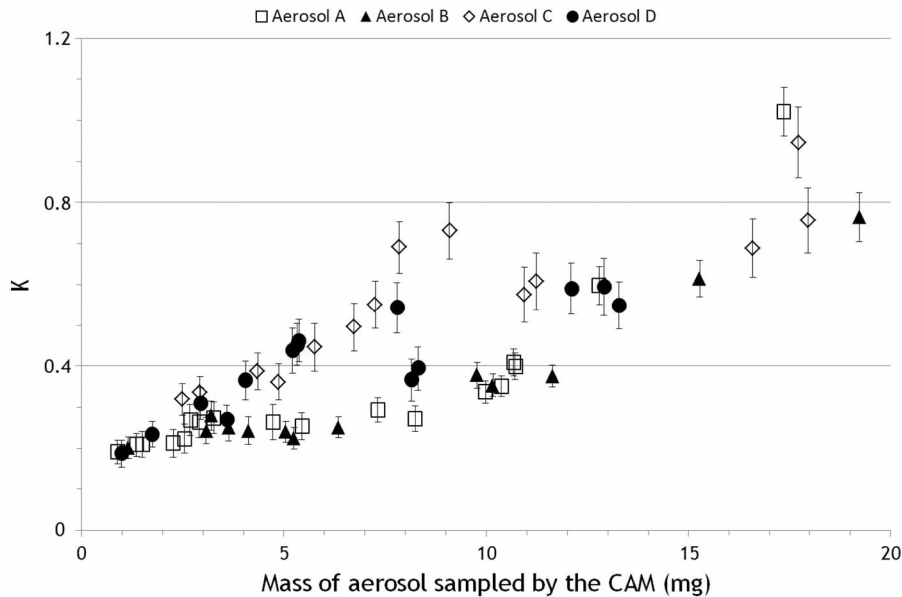


Fig. 6. Evolution of the K parameter related to the particle mass sampled for the non-radioactive aerosols A (□), B (▲), C (◇), and D (●).

comparable mass, the quantity of matter on the radiation path has a significant influence, and we can reduce the quantity to a volume and height and finally a number of particle layers.

To calculate the volume from the mass, we have to evaluate the packing porosity of the deposit. This parameter considers a deposit composed of solid particles “randomly” stacked in the air and not some continuous material. For that purpose, we use the empirical equation determined by Yu et al. (1997). Packing porosity represents the ratio of the empty volume to the particles’ volume in the structure formed on the filter. The packing porosity is 60% for aerosol A, 56% for B, 52% for C, and 45% for D. The larger the particle size is, the more compact the deposit is. We must consider spherical particles to evaluate the packing porosity. Moreover, we must also consider perfectly homogeneous particles deposited on the filter.

This volume leads trivially to the height of the deposit. The equivalent number of layers (N_{eq}) is then calculated using eqn (6):

$$N_{eq} = \frac{m_{acc}}{S_{eff} \rho MMV_{eq}D (1-\varepsilon)}, \quad (6)$$

where:

$MMV_{eq}D$

m_{acc} = particles mass collected on the sampling filter;

S_{eff} = effective particles in the deposit area of the sampling filter;

$MMV_{eq}D$ = mass median volume equivalent diameter, values reported in Table 1 for the four alumina aerosols used in this study; and

AQ9 ε = packing porosity calculated by using equation 2 of Yu et al. (1997).

The results are depicted in Fig. 7 for the four aerosols used. The number of particle layers grows linearly against masses, and the bigger the aerosol is, a smaller number of particles is needed to complete a layer. Indeed, at 13 mg, aerosol D (●) doesn’t even complete its first layer, whereas aerosol A (□) fulfils its third.

The transition zone in Fig. 6 for aerosols A and B is highlighted in Fig. 8 thanks to the calculated N_{eq} . This transition automatically leads to a higher distance inside the non-radioactive particles that the alpha particles travel through before reaching the detector. Thus, the higher the distance inside the non-radioactive particles, the higher the value of the K parameter.

An undistinguishable transition zone, in Fig. 6 for aerosols C and D, is confirmed in Fig. 9 thanks to the calculated N_{eq} . However, if the accumulated particle mass is sufficient, we think that the transition zone will occur. Indeed, when the N_{eq} is between 1 and 2 (only for the aerosol C surrounded by the dashed line in Fig. 9), the value of the K parameter seems to become higher.

However, the difference in the evolution trend between the two groups of results in Fig. 6 is not explained with the evolution of the number of particle layers on the filter. In the next section, different scenarios are discussed and could explain both the occurrence of the transition zone (linked to the N_{eq}) and the difference in the evolution trend of the K parameter related to the particle mass sampled.

Relation between the number of layers and the spectrum degradation

Fig. 10 illustrates the relations between the number of particle layers and the spectrum degradation for two particle sizes.

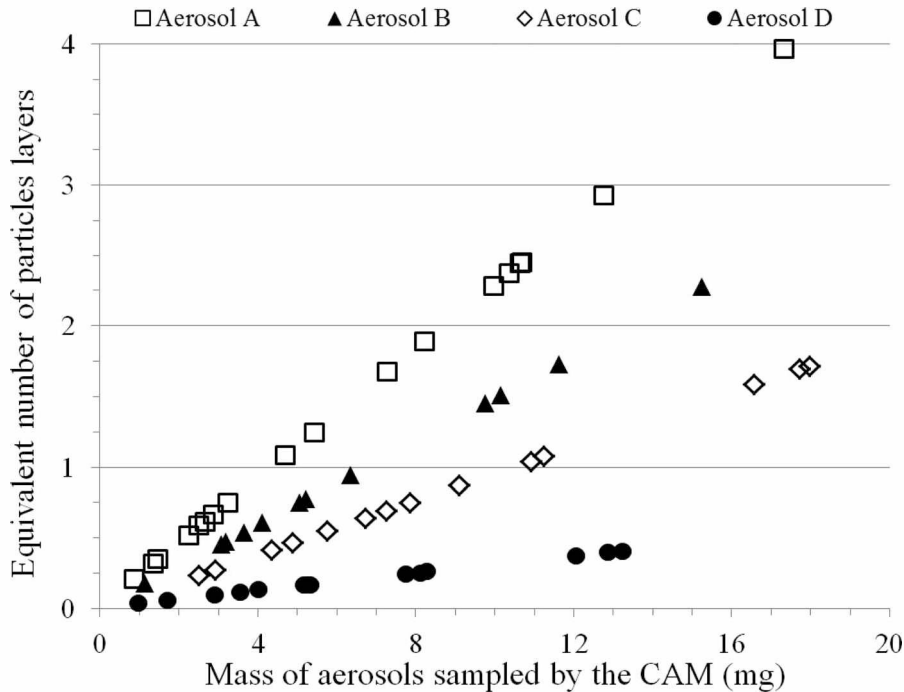


Fig. 7. Calculated equivalent number of particle layers on the filter depending on the mass of aerosols sampled for the four non-radioactive aerosols used: aerosol A (\square), aerosol B (\blacktriangle), aerosol C (\diamond), and aerosol D (\bullet).

For particle size below $10\ \mu\text{m}$ (from left to right and top to bottom in the upper box in Fig. 10), the particle deposition scenarios represent the configurations where $N_{\text{eq}} \leq 1$, $1 < N_{\text{eq}} \leq 2$, and $N_{\text{eq}} > 2$, respectively. In each of the three scenarios, the non-radioactive particles and the natural radioactive particles are represented by the black spheres (\bullet) and the small dashed spheres (\otimes), respectively. Black arrows show the alpha-particle path through the matter (particles, air)

to the detector. In the case of $N_{\text{eq}} \leq 1$, the non-radioactive particles constitute an uncompleted layer above the natural radioactive particles. Alpha-energy is impacted (alpha-energy attenuation is described in Knoll 2010) by this set of non-radioactive particles. Nevertheless, before the transition zone, only some alpha particles travel through a small distance inside the particles. The energy loss is therefore low. The energy spectrum is then slightly deteriorated, and this could

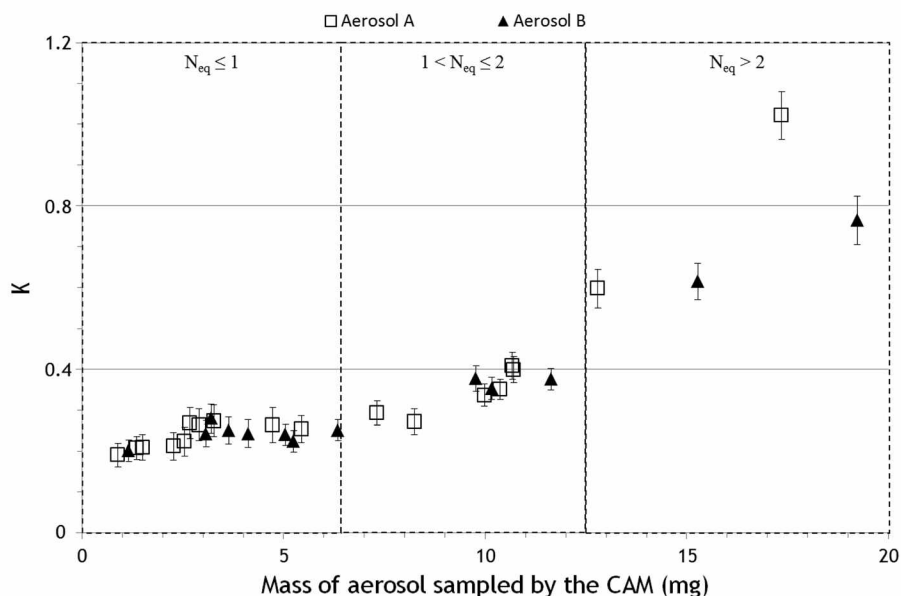


Fig. 8. Evolution of the K parameter depending on the mass of particles sampled by the CAM for aerosol A (\square) and B (\blacktriangle). Three zones that delimit the calculated N_{eq} are reported.

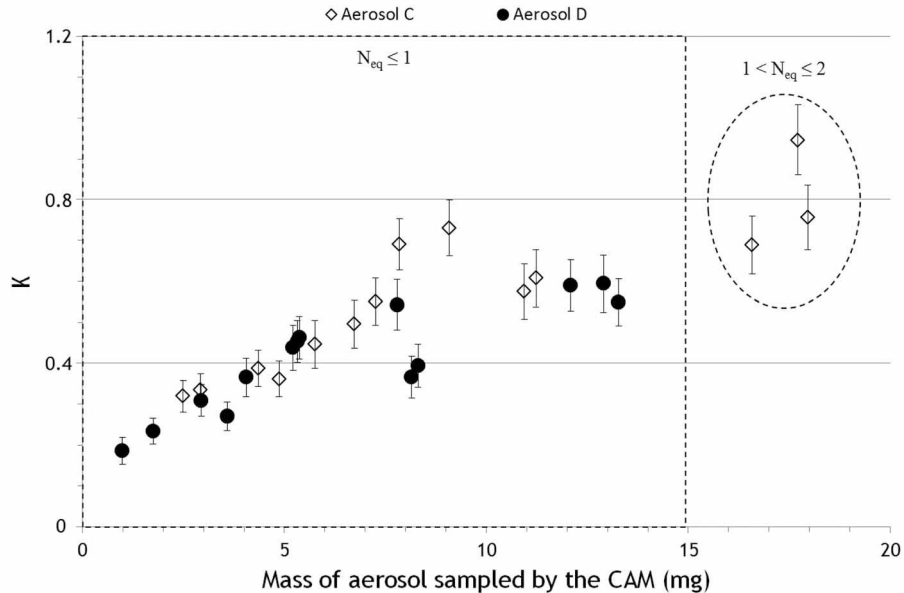


Fig. 9. Evolution of the K parameter depending on the mass of aerosols sampled by the CAM for aerosol C (◇) and D (●). The zone where the calculated N_{eq} is less or equal than one is delimited by the dashed square, while the three points surrounded by the dashed line are those where the calculated N_{eq} is >1 but <2 .

explain the small increase of the K parameter depending on the mass of particles sampled. Once the particle layer is almost completed, transition zone $1 < N_{eq} \leq 2$ is reached. In this case, the distance that the alpha particles travel inside the non-radioactive particles is higher, as they can sometimes travel longer than one layer of particles. Consequently, due to the higher energy loss inside the non-radioactive particles, the energy spectrum is a bit more deteriorated than in the case of $N_{eq} \leq 1$ and could explain the beginning of slope change

depicted in Fig. 8. Finally, when the N_{eq} is >2 , a lot of alpha particles travel more than one layer of non-radioactive particles and lead to an important energy attenuation. This energy attenuation could explain the fast increase of the K parameter, depicted in Fig. 8, in the case $N_{eq} > 2$.

For coarse particles, let's say with a $MMV_{eq}D$ higher than $10 \mu\text{m}$ (from left to right and top to bottom in the lower box in Fig. 10), the particle deposition scenarios represent the configurations where $N_{eq} \leq 1$ and $1 < N_{eq} \leq 2$, respectively.

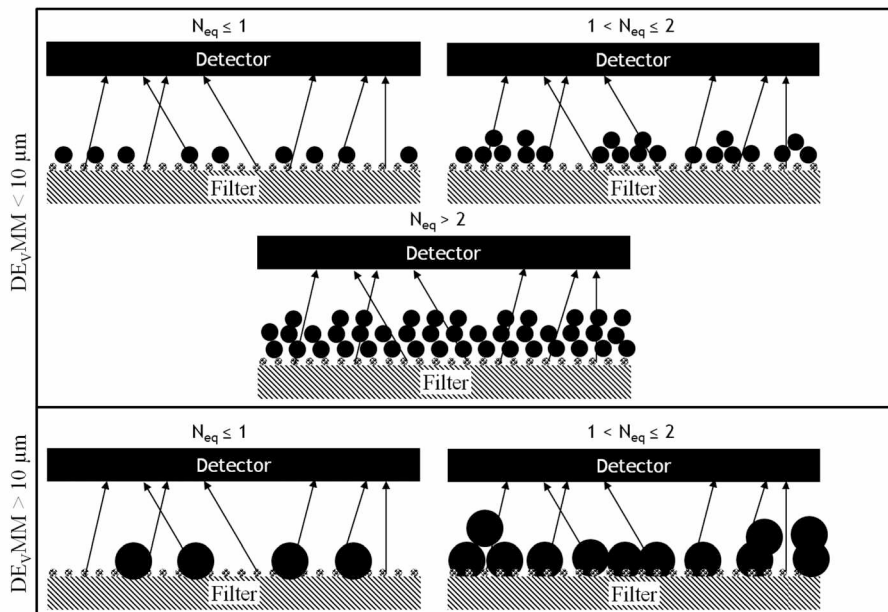


Fig. 10. For the particles with $MMV_{eq}D < 10 \mu\text{m}$, three schemes of particle deposition on a membrane filter are depicted in the upper box. For the particles with $MMV_{eq}D > 10 \mu\text{m}$, two schemes of particle deposition on a membrane filter are depicted in the lower box. Non-radioactive particles and natural radioactive particles are represented by the black spheres (●) and the small dashed spheres (⊗), respectively. Black arrows show the alpha-particle path to the detector.

In this case, fewer particles are necessary to reach the same mass of particles sampled on the filter. Nevertheless, even if the number of particles sampled is lower for a given mass, the space occupied is greater. The quantity of alpha particles traveling through non-radioactive particles is then greater. Moreover, the distance travelled by the alpha particles inside a non-radioactive particle layer is higher. When assuming these two latter parameters, this scenario could explain the fast increase of the K parameter, depicted in Fig. 9, even from the beginning of the accumulation mass of particles, which correspond to the case $N_{eq} \leq 1$.

Is the evolution of the K parameter impacted by the penetration profile of the natural radioactive aerosols?

The evolution of the K parameter for the two MMV_{eqD} cases presented here is in fact an average evolution over 2 h related to the mass of non-radioactive particles sampled in less than 10 min. The schematic explanations presented previously assume each time that the natural radioactive particles are always sampled on the surface membrane filter. This is true even if a cake of non-radioactive particles characterized by the packing porosity is formed at the surface of the filter. However, as the energy of alpha particles is greatly attenuated by their travel through the matter, the location of the natural radioactive particles is the relevant information. The penetration profile of the natural radioactive particles, depending on the sampled non-radioactive particle characteristics, could be a helpful parameter to improve the knowledge of the evolution of the K parameter in real time. This point will be investigated in the future.

CONCLUSION

The Continuous Air Monitor (CAM) measures in real time the alpha-artificial airborne activity while considering the influence of the background due to the radon progenies (especially ^{218}Po) on the measurement. This is achieved using a parameter, K, determined for IEC standard conditions. Even in a modern algorithm based on ROI and compensation, the K value is fixed for all exposure situations (e.g., 0.09 for the ABPM203M studied here). As soon as the exposure situation of the CAM is outside the IEC standard conditions, the fixed value of K is not suitable anymore. Indeed, the experimental results highlight an increasing trend of K related to the particle mass sampled on the sampling filter. Our results give a relationship between the K values and the accumulated mass and recommend a method to unfix the K values. Moreover, we highlight that not only is the accumulated mass required to determine the K values but also the aerosol size-distribution. Indeed, we establish four different relationships between K and the accumulated mass for four aerosol sizes.

On the other hand, the relation between K and the accumulated mass is different for the four aerosol sizes studied

here. It means that the mass accumulation of particles sampled is not the only parameter that impacts the behavior of the CAM. In the lower MMV_{eqD} case ($<10 \mu\text{m}$), a transition zone during the mass accumulation is distinguishable. Before the transition zone ($1 < N_{eq} \leq 2$), the increase of K related to the mass accumulation is small but constant. The slope of this increase suddenly becomes higher once the transition zone is reached. This behavior is explained by the change of the number of particle layers (N_{eq}) sampled on the filter; three zones that delimit the calculated N_{eq} are reported to the evolution of K as a function of the particles mass sampled, and the presence of a transition zone is highlighted.

In the higher MMV_{eqD} case ($>10 \mu\text{m}$), K increases quickly from the beginning of the aerosol sampling process. However, the number of particles layer is lower than 1, which does not explain this behavior. In this case, the space that the coarse particles take up is greater than the other MMV_{eqD} case for a given accumulated mass of particles. Consequently, the alpha particles have statistically more chance to travel through non-radioactive particles to reach the detector. In addition, the distance traveled inside the non-radioactive particles is higher. These two combined parameters could explain the sharp behavior of the evolution of K, even when the number of particles layer is lower than 1.

The knowledge of non-radioactive airborne particle characteristics is henceforth essential to better understand the energy spectrum shapes, notably outside IEC standard conditions. Indeed, the packing porosity, which is related to the particle size distribution, could be understood in addition to the mass of particles. In summary, a better background estimation into the ROI could be reached and false positives avoided.

REFERENCES

- Ammerich M. Réalisation d'une installation d'étalonnage de moniteurs de contamination atmosphérique à l'aide d'aérosols radioactifs calibrés (ICARE). CEA-R-5484; 1988.
- Baron PA, Willeke K. Aerosol measurement, principles techniques and applications. New York: Wiley; 2001.
- Bartlett W, Walker BA. The influence of salt aerosol on alpha radiation detection by WIPP continuous air monitors. In: Proceedings of the 24th DOE/NRC Nuclear Air Cleaning and Treatment Conference 1996: 000-000. **AQ10**
- Burghoffer P, Charau J, Merelli M, Prigent R. Method and portable carrying-out device for detecting atmospheric contamination by means of alpha particle aerosols. Patent No. EP 0128827 B1; 1987. **AQ11**
- Charau J, Pescayre G, Prigent R. Moniteur individuel de la contamination atmosphérique alpha (Type Monica α). Radioprotect 19:1-13; 1984 (in French). **AQ12**
- Cheng YS, Barr EB, Marshall IA, Mitchell JP. Calibration and performance of an API Aerosizer. J Aerosol Sci 24:501-514; 1993.
- Dougniaux G, Monsanglant-Louvet C, Teppe A-L, Marcillaud B, Dieux Lestaevl B, Gensdarnes F, Michielsen N, Bondiguel S, Boussetta B, Quentel G. Results from a measurement campaign in dismantling nuclear sites: a study of the false alarms emitted by CAM. In: Proceedings of the European Aerosol Conference 2016: 000-000. **AQ13**

- AQ14** Elder JC, Conzales M, Ettinger HJ. Plutonium aerosol size characteristics. *Health Phys* 27:000–000; 1974.
- Geryes T, Monsanglant-Louvet C. Determination of correction factors for alpha activity measurements in the environment (conditions of high dust loading). *Radiat Protect Dosim* 144:659–662; 2011.
- Hoarau G, Dougniaux G, Gensdarmes F, Dhieux Lestaevél B, Laurent J, Cassette P. Qualification d'un dispositif expérimental permettant l'étude d'un moniteur de la contamination atmosphérique dans des conditions représentatives de chantiers de démantèlement. *Congrès Français Sur Les Aérosols*; 2019 (in French).
- Hogue MG, Gause-Lott SM, Owensby BN, Slack TM, Smiley JJ, Burkett JL. alpha air sample counting efficiency versus dust loading: evaluation of a large data set. *Health Phys* 114:479–485; 2018.
- Hoover MD, Newton GJ. Performance testing of continuous air monitors for alpha-emitting radionuclides. *Radiat Protect Dosim* 79:499–504; 1998.
- Huang S, Schery SD, Alcantara RE, Rodgers JC, Wasiolek PT. Influence of dust loading on the alpha-particle energy resolution of continuous air monitors for thin deposits of radioactive aerosols. *Health Phys* 83:884–891; 2002.
- Justus A. Technical details of the sigma factor alarm method within alpha CAMs. *Health Phys* 120:442–453; 2021.
- Justus AL. Prompt retrospective air sample analysis—a comparison of gross-alpha, beta-to-alpha ratio, and alpha spectroscopy techniques. *Health Phys* 100:191–200; 2011.
- Klett A, Reuter W, De Mey L. Dynamic calibration of an aerosol monitor with natural and artificial alpha-emitters. *IEEE Trans Nucl Sci* 44:804–805; 1997. DOI:org/10.1109/23.603756.
- AQ15** Knoll GF. Radiation detection and measurement. In *Igarss 2014* (Issue 1); 2010.
- AQ16** Laraweb. Library for gamma and alpha emissions. 2017.
- Li H, Jia M, Wang K. Critical level setting of continuous air monitor. *Radiat Protect Dosim* 154:391–395; 2013.
- Mark D, Vincent JH, Gibson H, Witherspoon WA. Applications of closely graded powders of fused alumina as test dusts for aerosol studies. *J Aerosol Sci* 16:125–131; 1985.
- McFarland AR, Rodgers JC, Ortiz CA, Moore ME. A continuous sampler with background suppression for monitoring alpha-emitting aerosol particles. *Health Phys* 62:400–406; 1992.
- Monsanglant-Louvet C, Liatimi N, Gensdarmes F. Performance assessment on continuous air monitors under real operating conditions. *IEEE Trans Nucl Sci* 59:1414–1420; 2012.
- Moore ME, McFarland AR, Rodgers JC. Factors that affect alpha particle detection in continuous air monitor applications. *Health Phys* 65:69–81; 1993.
- Seiler FA, Newton GJ, Guilmette RA. Continuous monitoring for airborne alpha emitters in a dusty environment. *Health Phys* 54:503–515; 1988.
- Thomas JW. Measurements of radon daughters in air. *Health Phys* 23:783–789; 1972.
- Witschger O, Grinshpun SA, Fauvel S, Basso G. Performance of personal inhalable samplers operating in very slowly moving air and near the aerosol source. *Annals Occupat Hygiene* 48:351–368; 2004.
- Witschger O, Wrotel R, Basso G, Fauvel S, Gensdarmes F. Détermination expérimentale de facteurs de forme dynamique par comparaison des techniques Coulter et impacteur en cascade. *Congrès Français Sur Les Aérosols 2002* (in French). **AQ17**
- Yu AB, Bridgwater J, Burbidge A. On the modelling of the packing of fine particles. *Powder Technol* 92:185–194; 1997.
- Zettwoog P. ICARE radon calibration device. *J Research NIST* 95:147–153; 1990.



AUTHOR QUERIES

AUTHOR PLEASE ANSWER ALL QUERIES

- AQ1 = Please check if authors name are correctly captured for given names (in red) and surnames (in blue) for indexing after publication.
- AQ2 = Clarify “,,,sampled by the CAM on its behavior...”
- AQ3 = Verify author affiliation footnote is correct.
- AQ4 = Please confirm that the conflict of interest statement is still accurate.
- AQ5 = Include the address (city and state if within the US, and city and country if outside the US) for all vendors on first mention in the text.
- AQ6 = Is this change correct?
- AQ7 = The short title that the author provided exceeded 50 characters and spaces. Please check/revise the suggested short title.
- AQ8 = Provide the city and state (or city and country if outside the US) for all vendors on first mention in the text.
- AQ9 = Is “equation 2 of Yu et al. (1977)” the same as eqn 2 in this paper? If so, used “eqn” to refer to it here.
- AQ10 = References must be complete and in journal style as a condition of publication. See https://hps.org/documents/HPS_publications_style_guide.pdf and update reference list where citations are not complete. Also indicate if a citation is in French.
- AQ11 = For example, add city of publication and publisher to Ammerich 1988.
- AQ12 = For example, add city of publication, publisher and page range to Bartlett and Walker 1996.
- AQ13 = For example, add city of publication, publisher and page range to Dogniaux et al.
- AQ14 = Provide correct page numbers for Elder et al. 2011.
- AQ15 = Add complete citation for Knoll 2010.
- AQ16 = Add complete citation for Laraweb 2017.
- AQ17 = Add complete citation to Witschger.

END OF AUTHOR QUERIES